Grain-scale permeabilities of synthetic quartzite with volumetrically minor phlogopite, corundum, or aluminosilicate

Jonathan D. Price*, David A. Wark, E. Bruce Watson

Department of Earth and Environmental Sciences, Rensselaer Polytechnic Institute, 110 8th Street, Troy, NY 12180, USA

Abstract

In order to examine grain-scale permeabilities in materials that are microstructurally similar to those of the lower crust and upper mantle, we produced porous synthetic quartzites with small fractions of an additional minor mineral. Powdered quartz was mixed with minor amounts of either corundum or phlogopite and run in Ag capsules at 800–850 °C and 1.4 GPa for 5 to 10 days. The resulting quartzites generally exhibited microstructural equilibrium and contained phlogopite, corundum, or aluminosilicate. The minor mineral in all runs typically resided along quartz grain boundaries at low volume fractions (X) but increasingly occurred as porous clusters within corner pores at higher X. In all polished sections, the smallest quartz-bound pores appeared free of the minor mineral. Pore geometry of all materials differed from that observed in pure synthetic quartzite: pores exhibited an increased number of facets, a small decrease in the dihedral angle, and partial filling of larger pores by the minor phase. Measurements of permeability (k) were both higher and lower than those of monomineralic quartzite with similar ϕ, with k decreasing as a function of X. This decrease is likely the result of pore-throat reduction, either through fluid redistribution or obstruction of fluid pathways.
© 2004 Elsevier B.V. All rights reserved.

Keywords: porosity; permeability; grain-scale; microstructure; quartzite

1. Introduction

Many mass transport processes in the Earth involve the movement of fluids (C–O–H fluid and silicate, carbonate, or sulfide melt). Fluid transport has been linked to the rheological evolution of the deep crust and mantle (e.g. [1–3]), and fluid movement is coupled with mass and energy transport (e.g. [4]), including melt-extraction rates (e.g. [5–8]) and fluid–rock interaction (e.g. [9,10]). In contrast to the shallow lithosphere, where fluids may be transported through brittle fractures, interconnected grain-scale pores are likely pathways for fluid transport in the ductile regions of the lower crust and upper mantle.

---

* Corresponding author. Tel.: +1 518 276 2372; fax: +1 518 276 6680.

E-mail address: pricej@rpi.edu (J.D. Price).

Relatively high mineral solubility and favorable kinetics lead to rapid equilibration of pore microstructure in materials subjected to conditions appropriate for the lower lithosphere. The morphology of a fluid-filled pore is controlled in part by the energies of the two fluid–solid interfaces (γ_{sf}) and the solid–solid interface (γ_{ss}). Specifically,

$$\frac{\gamma_{s_1f}}{\sin\theta_2} = \frac{\gamma_{s_2f}}{\sin\theta_1} = \frac{\gamma_{s_1s_2}}{\sin\theta_3} \qquad (1)$$

where θ_1 and θ_2 are the angles between the crystal–crystal interface (grain boundary) and the two solid–fluid interfaces (pore walls), and θ_3 is the angle between pore walls (Fig. 1). If the two solid–fluid interfaces have identical and isotropic energies, then $\gamma_{s_1f}=\gamma_{s_2f}$, $\theta_1=\theta_2$, and θ_3 (hereafter simply θ) is the dihedral angle (Fig. 1), a measurable parameter. Thus, Eq. (1) may be arranged into its commonly cited form (e.g. [11–14]):

$$\cos\left(\frac{\theta}{2}\right) = \frac{\gamma_{ss}}{2\gamma_{sf}} \qquad (2)$$

This relationship defines the geometry of the fluid phase along grain boundaries (where two crystals join), along grain edges (where three crystals join), and at grain corners (where four or more crystals join). Because it is energetically favorable for volumetrically minor fluid to become localized at the grain corners and edges, fluids tend to be distributed in a network that may become connected depending on the

Fig. 2. Diagram showing a single idealized grain from a polymineralic material in textural equilibrium with a low volume fraction (ϕ) of fluid (modified from Watson and Brenan [1]). The quartz grains and pores of Wark and Watson [16] resemble this diagram. Outlined boxes on grain refer to (a) and (b), sections though grain-edge pore and grain corner pore. (a) Midsection of a pore along the junction of three grains showing the two-phase (quartz and fluid) dihedral angle (θ) determined by the ratio of the energies of the grain boundary with the two pore boundaries (see Eq. (2)). In this idealized system, this section is the smallest pore. (b) Planar section of a pore at the intersection of more than three grains.

dihedral angle and the volume fraction of the fluid. If the dihedral angle is greater than $60°$, pores are isolated from each other at low fluid fractions (ϕ) and will not form a connected network until ϕ is sufficiently large that the pores overlap. However, if θ is below $60°$, then the pores interconnect along grain edges at all ϕ in the fashion illustrated in Fig. 2 [11]. Although Eq. (2) describes an ideal system, it has been employed to describe materials that develop near-isotropic surface energies along solid–solid and fluid–solid interfaces, including some largely monomineralic rocks in equilibrium with aqueous fluid, such as quartzite, marble, and dunite.

Von Bargen and Waff [15] used the geometrical relationship dictated by Eq. (2) to predict that the permeability (k) should scale to the square of ϕ for θ
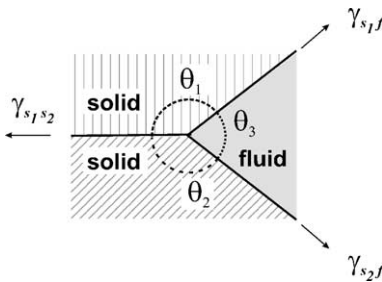

Fig. 1. Two-dimensional depiction of equilibrium between a grain boundary and pore (i.e. two equal fluid–solid boundaries), modified from Smith [11]. The parameters, also used in Eq. (1), include the surface energies of the fluid–solid boundary (γ_{s_1f}, γ_{s_2f}) and the solid–solid boundary ($\gamma_{s_1s_2}$), and the angles between these boundaries (θ_1, θ_2, θ_3). The angle between the pore walls, θ_3 is known as the dihedral angle.
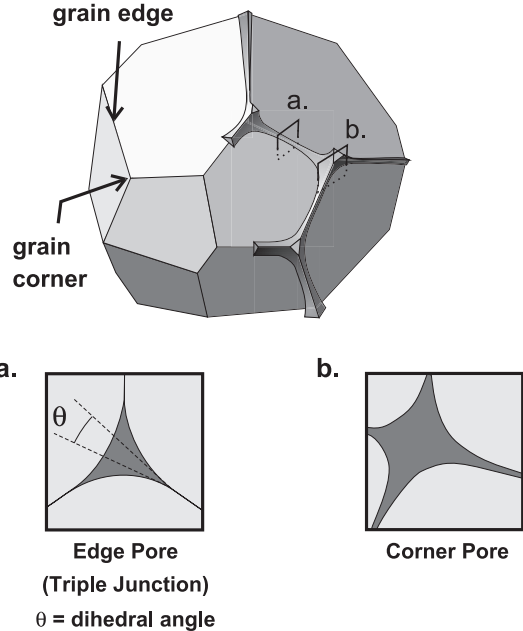
<60° in an idealized system composed of uniform grains and pores. More recently, Wark and Watson [16] characterized the $k–\phi$ relationship for systems consisting of non-uniform grains and pores by directly measuring the permeability of synthetic quartzites with variable volumes of water and brine ($\theta<60°$) and marbles with variable volumes of water ($\theta>60°$). The results of their study were modified slightly by Liang et al. [14] to account for the small amount of molecular slippage inherent to near-atmospheric pressure gas permeability measurements (see Dullien [17]), thus yielding the following equation for quartzites:

$$k = \frac{d^2\phi^3}{270} \qquad (3)$$

This equation serves as a good approximation for the $k–\phi$ relationship in monomineralic, microtexturally equilibrated materials with pores similar to those shown in Fig. 2, and serves as an ideal model fluid movement in the deep lithosphere. However, most materials of the deep lithosphere are not entirely monomineralic; even in nominally monomineralic lithologies, such as quartzite and marble, one finds small fractions of other minerals. How such deviations in texture affect permeability are not presently understood and prompted this investigation.

Theoretically, the addition of a second, volumetrically minor mineral may affect pore morphology in a several ways. For example, addition of a second solid phase should locally change the grain boundary energies (γ_{ss}) (see [18] and references therein), potentially altering the dihedral angle. And the additional dissolved components of the minor mineral in the fluid may also affect the pore–wall boundary energies (γ_{sf}), again potentially resulting in a change in the dihedral angle (e.g. [1,19]) or promote faceting (e.g. [20]). At the extreme, the minor mineral may even localize to pores and physically obstruct the fluid network.

Because permeability is dependent on pore morphology, such excursions from the idealized pore structure might result in a $k–\phi$ relationship different from that relevant to monomineralic materials. To evaluate the influence of a minor mineral on the $k–\phi$ relationship, we measure permeabilities of synthetic porous quartzites containing a minor solid phase and compare these measurements with those of Wark and Watson [16]. While our quartzites remain much simpler than most lithospheric materials, they permit investigation of the effect of an additional volumetrically minor mineral on grain-scale permeability, which more closely approximates earth materials. We show that addition of the second solid phase does demonstrably change the pore morphology from those within the quartzite–fluid materials. Correspondingly, this alters the $k–\phi$ relationship.

2. Methods

2.1. Rock synthesis

The synthetic quartzites with minor mineral phases were synthesized from optically clear natural quartz (Wards cat. #45 W 9207) crushed to a <22 μm grain size, mixed with small amounts of either 0.3 μm synthetic corundum (αAl_2O_3 powder—Alpha Resources cat. #AM0782) or <5 μm synthetic fluorophlogopite (produced from oxides and fluorides at 800 °C, 1 GPa). These powders were ground in an agate mortar and pestle under ethyl alcohol for 30 min, dried, and further mixed by tumbling overnight. The powder mixtures were loaded into cylindrical Ag containers (length 8 mm, o.d. 6 mm, i.d. 5 mm; Fig. 3a). Fluid was added to the powder with a micro-syringe in prescribed amounts to control the sample porosity (ϕ). The fluid was either doubly distilled H_2O (corundum-added runs) or 4 M HF (in phlogopite-added runs, to exploit the relatively higher thermal stability of fluorophlogopite, as in [21]). Most runs, particularly those of low porosity ($\phi<0.02$), were surrounded by an additional molybdenum ring covering the center 4 mm of the Ag capsule to limit quench deformation of the sample. A flat Ag lid was placed on top of the container, and the container and lid were positioned in the piston-cylinder assembly (Fig. 3b). Upon cold pressurization, the lid formed a seal against the container rim that survived subsequent heating to the peak temperature. Corundum-added quartzite runs (Dc series) were synthesized at 850 °C and 1.4 GPa for 5 or 10 days, while phlogopite-added quartzite runs (Ph series) were synthesized at 800 °C and 1.4 GPa for 5 days. All runs were rapidly quenched to

<100 °C in 20 s or less by cutting power to the furnace.

2.2. Permeability measurements

Following quench, the cylindrical metal containers were removed and sawn perpendicular to the capsule axis at both ends to expose the synthetic rock (Fig. 3c). The Ag or Mo-girdled-Ag container was retained as a jacket to maintain sample geometry and provide sealing surfaces to contain gas flow in the rock during permeability evaluation. The sample was dried, pushed into Tygon tubing, and then inserted between two polished aluminum fittings. The fittings and tube-jacketed sample were positioned in the permeameter sample vise, confining them at $P > 2.0$ MPa such that the Tygon formed a gas-tight seal with fittings and the fittings formed a gas-tight seal with the rubber o-rings of the vise (Fig. 3d). A hole in each of the two vise end-plates and in the fittings permitted gas transport to each exposed end of the rock from the two gas reservoirs, such that the adjoining gas reservoirs communicated solely through the sample pores.

Pulse decay permeametry requires the measurement of the pressure equilibration over time between two reservoirs initially at different pressures (see [14]). For this work, we used an Ar permeameter with an upstream volume (V_1) of 78.8 ml and a downstream volume (V_2) of 342.4 ml (a slightly modified version of the device described in [16]). An Omega PX 181 transducer measured the upstream pressure (P_1), and a Honeywell ST3000 differential transducer measured the difference in pressure between the two reservoirs ($\Delta P = P_1 - P_2$, where P_2 is the downstream pressure). Changes in P_1 and ΔP were recorded over time using an Omega OM-160 digital datalogger and associated MS DOS software. Limitations of this device stipulate that: P_1 must be greater than P_2, the initial upstream pressure ($P_{1,0}$) cannot exceed 1.5 MPa, and ΔP cannot exceed 0.69 MPa. Most samples were analyzed at $P_{1,0} = 1.2$–1.4 MPa and $P_{2,0} = 0.8$–1.0 MPa (initial downstream pressure), which are optimal conditions for our permeameter [14]. All samples were analyzed at least twice with a new Tygon jacket and aluminum fittings to test the reproducibility of the decay curve.

The change in ΔP over time produces a decay curve (from $\Delta P = P_{1,0} - P_{2,0}$ to $\Delta P = 0$); decay times ranged from 5 min to 1 week. Sample permeability is related to the slope of the decay curve [22]. For our calculation, we used Eq. (5) of Liang et al. [14]:

$$\frac{P_1 - P_2}{P_{1,0} - P_{2,0}}$$
$$= \frac{\left[(P_{1,0} + P_{2,0} + 2b)(V_1 + V_2) - (P_{1,0} - P_{2,0})(V_2 - V_1)\right]F(t)}{(P_{1,0} + P_{2,0} + 2b)(V_1 + V_2) - (P_{1,0} - P_{2,0})(V_2 - V_1)F(t)}$$

(4a)

and

$$F(t) = \exp\left\{-\left[\frac{1}{V_1} + \frac{1}{V_2}\left(\frac{P_{10} + b}{P_{20} + b}\right)\right]\frac{A(P_{20} + b)k}{L\mu}t\right\}$$

(4b)

where t is time in seconds, b is the Klinkenberg slip parameter in bars, A is the cross-sectional area of the sample quartzite cylinder in cm^2, L is the length of the cylinder in cm, k is the permeability, and μ is the shear viscosity of the gas medium (Ar). For samples with log $k > -18$, such as those in this study, employing $P_{1,0} > 1$ MPa as we did, b is negligible and is set to zero for all of our calculations (see [14]). Because many samples equilibrate rapidly and preclude accurate observation of the initial pressures ($P_{1,0}$ and $P_{2,0}$), we calculated these parameters by applying a polynomial fit to the differential pressure decay curve and extrapolating the intercept P values. Curve fits to $(P_1 - P_2)/(P_{1,0} - P_{2,0})$ vs. t produced a value for the pressure–volume term employed to approximate the permeability, k.

2.3. Grain size characterization

Following permeametry, the samples were axially sectioned (Fig. 3e) and examined using a JEOL 733 electron microprobe in SEM mode. The compositions of the minor minerals were determined by energy-dispersive X-ray spectrometry (EDS).

In order to compare permeability values between samples of different grain size, we normalized all measured k values to a 1 mm grain diameter. Grain size for each product was measured on three or more secondary and backscattered electron micrographs containing 150–400 grains each, for a total of at least 1000 grains per sample. Characterization used the
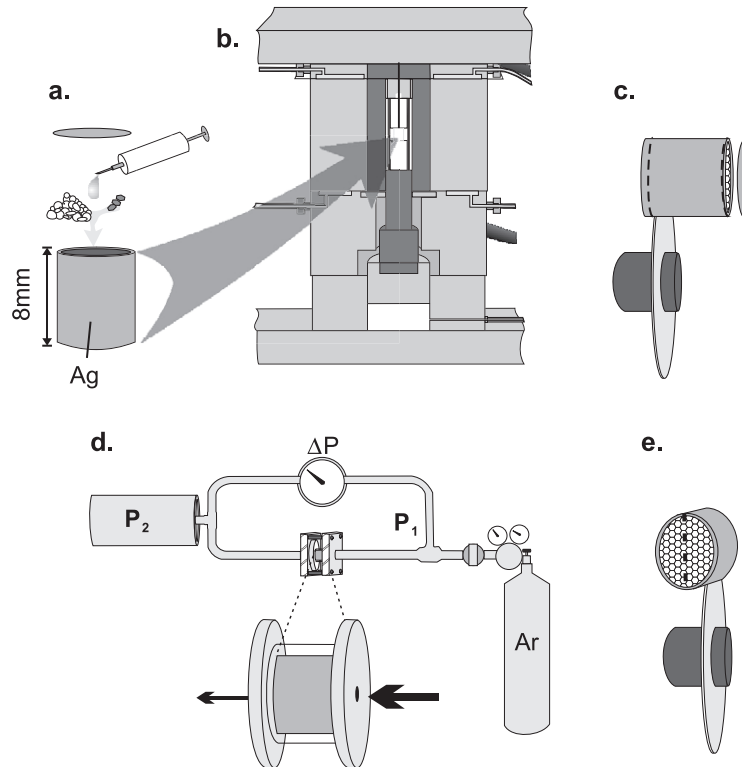
Fig. 3. Schematic representation of experiment assembly, post-run preparation, permeability analysis, and preparation for visual analysis. (a) Powders of quartz and a minor solid phase are homogenized and loaded into an Ag cylinder, into which are injected H_2O or dilute HF in amounts appropriate for a given fluid fraction (ϕ). (b) Capsule is surrounded by MgO (insulation and pressure medium), and placed within a NaCl-pyrex-jacketed graphite furnace, positioned in the piston cylinder apparatus, pressurized to 1.4 GPa, and heated to 800 °C (Ph series) or 850 °C (Dc series). (c) Following quench after 5 or more days, samples are extracted and sawn to expose product at each end of the cylinder. (d) The cylinder is jacketed with Tygon tubing and each end is press fit into aluminum fittings designed to couple with the permeameter. The jacketed cylinder and end caps are clamped into a retaining vise in the permeameter such that the sample is the sole pathway between a pressure differential. (e) Following permeability analysis, the sample is sectioned for examination and grain-size characterization.

same volume-based, grid and line-sampled intercept stereographic techniques [23,24] employed by Wark and Watson [16].

3. Results

3.1. Experimental products

We designed each experiment to produce a synthetic quartzite equilibrated with fluid and with a small volume of an additional, finer-grained solid phase. Here, with two noted exceptions, we report only those runs that approached an equilibrated microstructure (based on uniformity of grain size

and pore distribution), contained no glass (i.e. melt at run conditions), and lacked fractures oriented such that they might influence gas flow during permeability evaluation.

Attainment of an equilibrated microstructure was assessed from the grain size distribution (GSD) of quartz crystals. Crystalline grains in metals, alloys, ceramics, and rocks are considered texturally equilibrated if they exhibit a constant GSD over time [25–27]. The apparent GSD determined from a section plane is a valid assessment of the true GSD, although the apparent average diameter of sectioned grains may be as little as 90% of the actual value [28]. Test samples, similar to those materials synthesized for this study, yielded a constant GSD after 72 h (sometimes

appreciably faster at relatively high fluid fraction, ϕ). The materials in this study are thought to contain near equilibrium microstructures because (1) they were all held at peak conditions for periods exceeding 72 h, and (2) the products exhibit GSDs characteristic of an equilibrated material. Exceptions may include the two products with the highest fraction of corundum (X) and lowest ϕ (see Section 3.1.1).

All runs contained a number of fractures resulting from post-run axial decompression. These fractures are subparallel to one another and normal to the axis of unloading stress in the piston cylinder apparatus. Because we aligned the cylindrical axis of the material with the axis of decompression in the piston cylinder, and because Ar flow in the permeameter was along the same axis, these cracks did not greatly influence the pressure decay rate because they merely extend the sample.

Sample compositions, experimental conditions, and the results of permeability measurements for each successful run are presented in Table 1. With the exception of two runs, DcF and Ph26, ϕ was calculated using the mass of fluid added to the capsule immediately prior to each run, dividing this value by the ideal density of the fluid calculated for the run

conditions (using the equations of Belonoshko and Saxena [29]), and determining the ratio of the volume of the fluid to the total volume of components. Modal calculation of pore fractions using electron micrographs of polished surfaces verified these calculated values for all but two samples. Modal analysis of runs DcF and Ph26 yielded significantly lower fluid fractions compared to those calculated from the added components, suggesting fluid loss during sample synthesis. This is most likely due to evaporation prior to pressurization. Thus, we report the fluid fractions as those determined by image analysis for these two products only.

In both methods of pore assessment, ϕ represents the total fluid volume fraction, not necessarily the interconnected fluid fraction (ϕ_i) that contributes to the permeability. However, as in the quartzites synthesized by Wark and Watson [16], all products contained low dihedral angles and a relatively uniform distribution of pores observed in the polished sections, suggesting that pores should be interconnected.

The volume fraction of the minor mineral phase (X), also reported in Table 1, is calculated from the volume of minor-phase component added to the starting powder over the total volume of the materials

Table 1
Starting materials, conditions, and results for each experiment

Sample	Run duration	Qz grain diameter d	Fluid added	Qz added	Platy added	Fluid fraction ϕ	Minor fraction X	Minor mineral[a]	Sample diameter D	Sample length L	Normalized Permeability[b] k
	(days)	(μm)	(mg)	(mg)	(mg)				(cm)	(cm)	(m²)
Quartz+corundum+H_2O (850 °C, 1.4 GPa)											
Dc13	10	23.9	6.90	213.32	6.58	0.078	0.018	crn	0.55	0.33	1.51e−12
Dc14	10	20.2	2.30	202.55	6.25	0.029	0.019	crn	0.55	0.33	1.78e−13
Dc15	5	18.2	0.62	197.80	6.10	0.008	0.020	crn	0.52	0.43	3.02e−14
DcF	5	12.2	1.99	179.45	13.51	0.020	0.046	crn	0.46	0.43	8.47e−15
DcM[c]	*5*	*13.7*	*0.92*	*170.78*	*12.85*	*0.013*	*0.047*	*crn*	*0.48*	*0.36*	*1.10e−14*
DcJ	5	27.6	5.91	177.66	13.37	0.077	0.044	als	0.46	0.38	2.82e−13
Dc17	5	25.2	5.60	163.96	18.14	0.077	0.068	als	0.50	0.25	1.61e−12
Dc19	*5*	*11.4*	*1.00*	*176.91*	*19.66*	*0.014*	*0.067*	*crn*	*0.46*	*0.39*	*1.07e−15*
Quartz+phlogopite+4 M HF (800 °C, 1.4 GPa)											
Ph24	5	20.26	1.75	181.40	5.60	0.024	0.028	ph	0.50	0.32	4.46e−14
Ph25	5	21.37	6.62	185.47	5.72	0.084	0.028	ph	0.47	0.41	1.74e−12
Ph28	5	21.90	5.35	170.07	5.25	0.075	0.026	ph	0.48	0.45	5.97e−13
Ph34	5	15.33	0.96	171.46	5.30	0.015	0.027	ph	0.47	0.23	3.59e−14

[a] Minor mineral precipitated in run products, crn=corundum, als=aluminosilicate, and ph=phlogopite.
[b] Reported value is permeability normalized to a grain diameter of 1 mm, using $k=(1000/d)^2*k_m$, where d is in μm and k_m is the permeability determined through in Eq. (4).
[c] Italics denote these samples exhibit a more complicated microstructure.

in each capsule (powder plus fluid). Like the fluid fraction, the actual volume of the solid components was not directly measured, but calculated by dividing the measured mass of each component by the average density of the phase in the run product, assuming a pure and stoichiometric composition for each phase. While the actual density of the solid and fluid components undoubtedly differs from the employed value, the calculated volume fractions (X or ϕ) do not change significantly over the range of plausible density values for each phase.

All run products used for permeability measurements contained three phases (quartz, a volumetrically minor mineral, and fluid, either H_2O or dilute HF) producing five interfaces: quartz–quartz, quartz–minor mineral, quartz–fluid, minor mineral–minor mineral, and minor mineral–fluid. All products contained a number of mineral–fluid interfaces that exhibited no curvature at the scale of the electron micrograph, and throughout the remainder of this paper we refer to these apparently flat pore boundaries as facets.

3.1.1. Corundum-added quartzites

Corundum-added mixtures (Dc series) produced a diverse set of products, each with a final texture and composition depending on the volume fractions of both the minor mineral (X) and of the fluid (ϕ). Only the two runs with the highest fluid fractions and elevated corundum fractions (Dc17 and DcJ) produced an aluminosilicate (als). Although the aluminosilicate was not structurally characterized, it was most likely kyanite, the phase calculated to be in thermodynamic equilibrium at run conditions. Aluminosilicate grains appeared tabular and euhedral (Fig. 4a and b) and were larger than any of the other minor-phase grains produced in this study, growing to apparent lengths of 30 μm. Most aluminosilicate grains occurred in clusters and were confined almost exclusively to large pores bounded by four or more quartz grains.

The rest of the corundum-added products contained substantially coarsened grains of corundum (crn). At the highest ϕ values (~0.08), corundum exhibited a bimodal distribution, with small, uncoarsened grains included in quartz and larger (3–15 μm apparent length) grains as clusters in the largest pores. At lower ϕ, a greater fraction of corundum grains
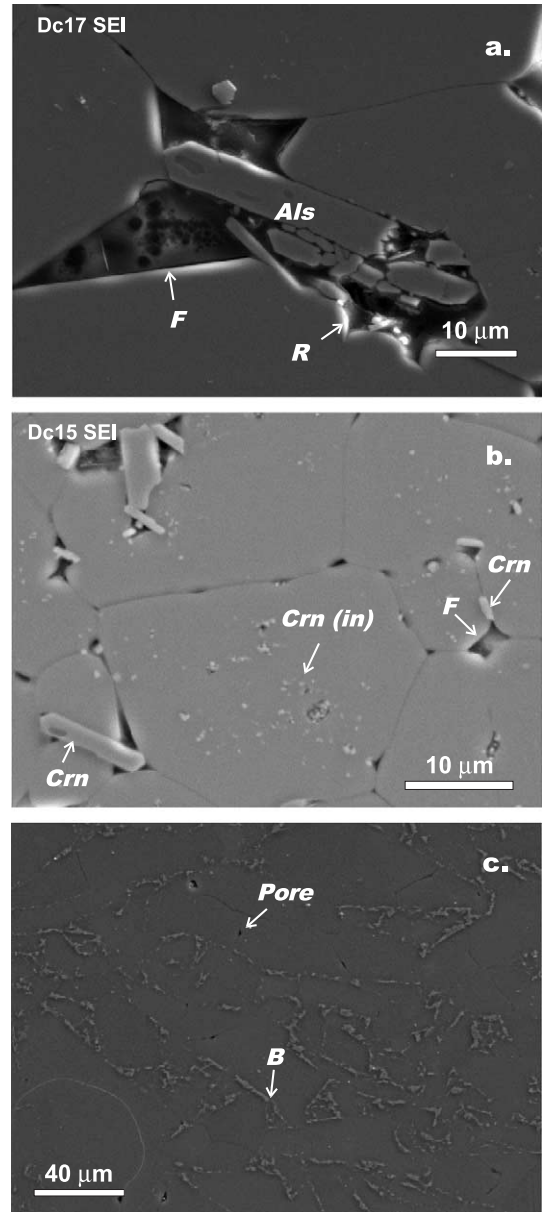

Fig. 4. Scanning electron micrographs of corundum-added products. (a) High-X (0.067), high-ϕ (0.079) product Dc17. Aluminosilicate, **Als**, exhibits tabular morphology within large pore. Note flat pore wall, **F**, and rounded pore wall, **R**. (b) Low-X (0.020), low-ϕ (0.008) product Dc15. Corundum (light gray, **Crn**) grains are located in many of along quartz grain boundaries and in pore spaces. Corundum is also present as small inclusions, **Crn (in)**, within the quartz grains. Note the presence of flat pore walls, **F**. (c) Moderate-X (0.047), low-ϕ (0.013) product DcM. Quartz crystals (dark gray) apparently outlined by corundum grains (light gray), **B**. Pores are small, and many are located at corundum-free quartz grain boundaries, **Pore**.

were high aspect ratio grains located on quartz grain boundaries, preferentially oriented with their long axes parallel to these boundaries, and jutting from these boundaries into pores. The higher X, lowest ϕ products, DcM and Dc19, were markedly different: corundum grains appeared little coarser than their 0.3 μm starting size (Fig. 4c) and were too small to evaluate their shape. Grains were predominantly located along quartz grain boundaries; there was no evidence of included grains and scant evidence of their presence in pores.

In addition to the noted variation in minor mineral distribution, the texture of the quartzite in our products differed as a function of both the fluid and corundum volumes. The mean grain size of quartz increased with decreasing minor mineral to fluid ratios (X/ϕ): the average diameter (d) ranged from roughly 10 μm for X/ϕ near 4, to 25 μm for X/ϕ less than unity. Quartz morphology also varied in proportion with X/ϕ. Low X/ϕ runs produced largely equant grains that, except for a larger number of facets, were similar to those produced in clean synthetic quartzite (cf. Fig. 5d in [16]). In contrast, the quartz grains within samples with elevated X/ϕ (DcM and Dc19) appeared largely bounded by corundum. Quartz exhibited irregularly shaped outlines (Fig. 4c), much like those in the compacted starting powder. A small number of boundaries were free of corundum and were loci for the larger pores.

3.1.2. Phlogopite-added quartzites

The same initial X (~0.03) was employed in all phlogopite-added experiments (Ph series). Consequently, the differences between the products were correspondingly less dramatic relative to those noted in the Dc series. All products contained small euhedral platy phlogopite (ph) crystals. Even within a single run product, there was an apparent bimodal nature to the phlogopite grain size and distribution, occurring both as clusters of numerous small crystals and as larger isolated grains. Much like the corundum-added materials, phlogopite within high ϕ products was typically located in larger pores throughout the sample (Fig. 5a), while phlogopite in low ϕ runs was largely distributed along quartz boundaries (Fig. 5b). Again, in this latter case, crystals were aligned along quartz grain boundaries and commonly extended into pores.
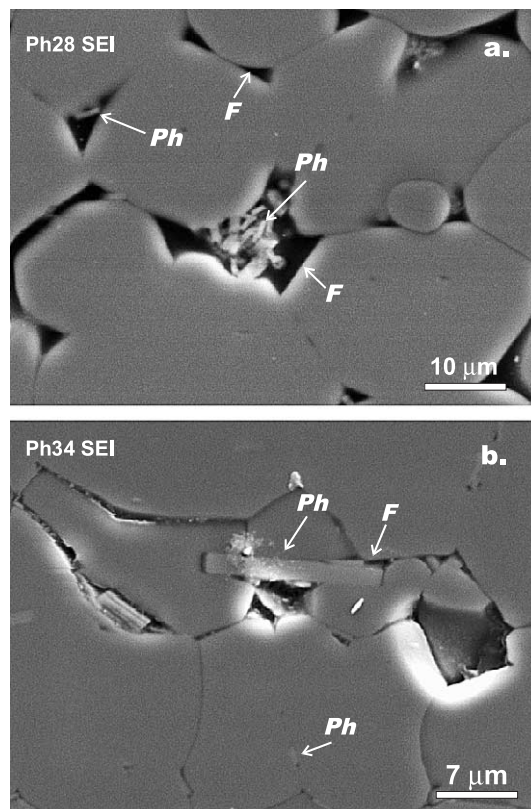

Fig. 5. Scanning electron micrographs of phlogopite-added products. (a) High-ϕ (0.078) product Ph28 with phlogopite, **Ph**, as clusters within larger pores and some individual grains within smaller pores. Note small pores within the cluster. Note also the large number of flat pore walls, **F**. (b) Low-ϕ (0.015) product Ph34 with phlogopite along quartz grain boundaries and within pores.

The texture of quartz in the phlogopite-bearing products was similar to corundum-added materials of comparable X. Equant quartz grains, with an apparent average grain size near 21 μm, dominated each Ph series run.

The overall texture of the phlogopite-added materials, particularly those at low ϕ, was reminiscent of examples of natural quartzite with small fractions of mica (e.g. [30,31]). In both natural and synthetic materials the mica grains were located predominantly along quartz grain boundaries and a number were located partially within pores, although the distribution of the minor mineral in our synthetic materials was more uniform than that typically observed in natural quartzite.
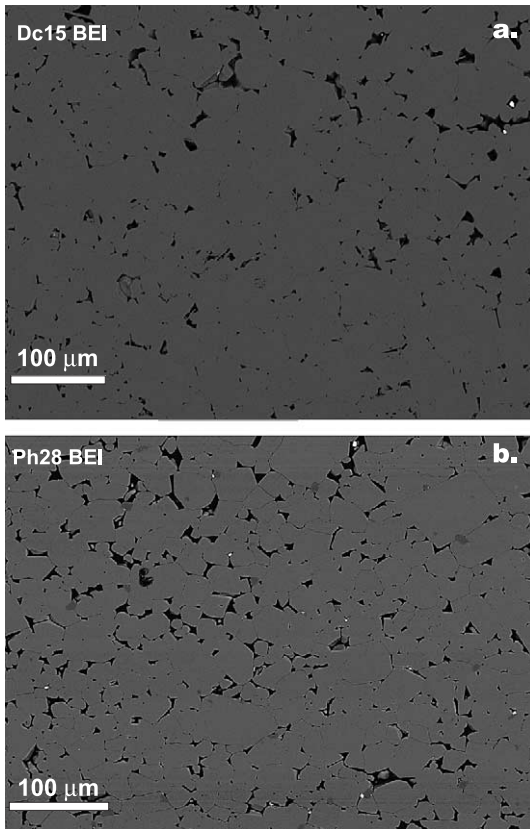
Fig. 6. Backscattered electron micrographs showing the general texture of run products. Solid phases are gray, epoxy- or air-filled pores are black. Bright spots are capsule material (Ag). (a) Corundum-added quartzite Dc15 showing relatively low concentrations (~35%) of flat pore walls. (b) Phlogopite-added quartzite Ph 28 showing relatively increased degree of flat pore walls (~70%).

3.1.3. Pore geometry

The pores within the quartzites produced in this study deviated from ideal morphology (such as Fig. 2a) and exhibited significant variability in shape. In the high ϕ materials, the minor minerals appeared as clusters in larger pores. These minor mineral clusters were porous in section (pores within clusters were generally a few tenths of a micron across, see Fig. 5a). At lower ϕ, minor mineral grains were more likely to be along quartz grain boundaries, protruding into pores. In either case, a significant fraction of pores appeared to include minor mineral grains, although the smallest pores were typically free of the minor mineral.

Although a number of the pore walls were curved, as anticipated from the ideal morphology (i.e. Fig. 2), many pore walls were flat. These were bounded either by the minor mineral or by quartz facets. Nearly 70% of pore–grain boundary junctions contained a faceted wall within phlogopite-added materials, compared to 35% in corundum-added materials (Fig. 6). The degree of faceting apparently depended on neither ϕ nor X, although we were unable to verify this in the low ϕ materials due to the small size of the pores. Apparent angles of faceted pore–grain boundary intersections were almost always acute and typically less than 60°.

In both series of experiments, the median value of the dihedral angle was slightly lower than observed in quartzite–fluid systems [19]. Using measurements from backscattered-electron micrographs of polished surfaces, the median of apparent angles for unfaceted quartz–quartz junctions in phlogopite-added products was 37°, and the median of angles in corundum-added materials was 34°, regardless of their respective aluminum-bearing phase. Both values are slightly smaller than those of the quartzite–brine (38°) and quartzite–water (44°) pores in Wark and Watson [16].
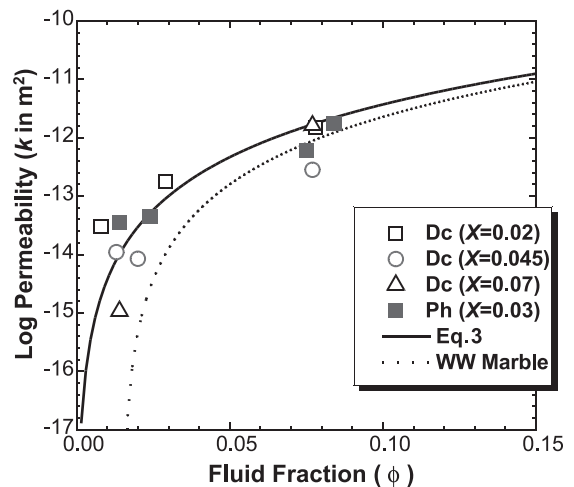

Fig. 7. Plot of the log of permeability (k) normalized to a 1-mm grain size versus fluid fraction (ϕ) for the products described within this paper. Series Dc (open symbols) refers to corundum-added materials, and series Ph (filled squares) to phlogopite-added materials. The solid line is the plot of Eq. (3), and the dotted line (WW Marble) refers to the fit determined from Calcite+Fluid (θ=68°) data from Wark and Watson [16].

3.2. Measured permeabilities

Permeability values (k) determined by pulse decay and normalized to a quartz grain diameter (d) of 1 mm are listed in Table 1 and plotted in Figs. 7 and 8 as functions of ϕ and X, respectively. In Fig. 7, the k values for a given ϕ straddle the Eq. (3) curve. Most k are within a factor of five of the relationship exhibited by pure synthetic quartzite for a given ϕ, defined by Eq. (3), except for two low and one high ϕ samples. Fig. 8 expresses our data in terms of k versus X normalized to three specific values of ϕ: 0.015, 0.025, and 0.077. For the $\phi=0.015$ data, Log k decreases from -13.4 to -14.9 m^2 as X increases from 0.020 to 0.067. The other two data sets are too small and erratic to evaluate in terms of X, but they generally mimic this relationship.

The source of error for k lies predominately within the physical measurements of the sample. Among the parameters used to calculate k from the measured decay curve (see Eq. (3)), those used to calculate sample volume (V) have the largest error, including the cross-sectional area (A), which may vary as much as 10% due to sample-wall deformation, and length (L), which may vary up to 5% due to plucking of

grains on end surfaces and extension cracks within the sample. Grain size analysis produced additional error (up to 5%): each sample was analyzed by visual determination of grain boundaries on highly magnified images, using around 1000 line samples per product. Multiple assessments of a few samples produced the same d within 1% of the average value in each case. In total, the analytical error on each measured k value is less than 50%.

4. Discussion

4.1. Microtexture and pore network formation

Prior to heating and pressurizing, all of our materials started as quartz fragments, minor mineral fragments, and fluid. These underwent kinetically controlled transformations typical of polycrystalline materials subjected to thermal and mechanical stress: compaction and densification followed by recrystallization (see [32]). In most cases the two solid phases coarsened and approached an equilibrium microstructure dominated by near-equant polygonal quartz grains and a fluid network, similar to that shown in Fig. 2. Grains of the minor mineral were distributed along quartz grain boundaries, in pores, and as inclusions within quartz grains. Such coarsening texture has been previously demonstrated in fluid-bearing systems composed of microcrystalline quartz and a minor mineral (e.g. [33]).

The low-ϕ, high X, corundum-added runs, DcM and Dc19, are noted exceptions. They possess a distinct microstructure with quartz grains largely bounded by an irregularly shaped outline of uncoarsened corundum grains. It is likely that coarsening of quartz in these two samples was greatly impeded by the grain-boundary pinning force (Zener drag) of the corundum particles (e.g. Zener in [11,18]). The irregular size and shape of the quartz grains in these two materials undoubtedly results in a more complicated pore distribution. Furthermore, the small fluid fraction likely formed a number of pores that were too small to assess on the electron microprobe. However, there are relatively large pores along quartz grain boundaries, particularly those that are free of corundum. Pores at these locations may have arisen along inter-grain fractures developed in quartz during
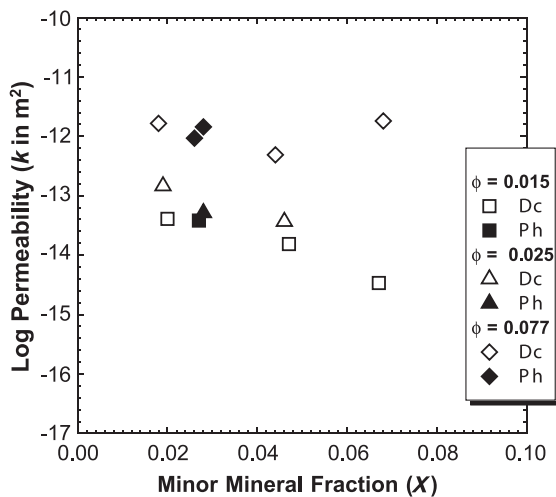

Fig. 8. Plot of the log of permeability (k) normalized to a 1-mm grain size versus fraction of the minor mineral (X) for our products. For comparison, the fluid fraction (ϕ) for each sample has been normalized to the closest of three values, 0.015, 0.025, and 0.077. Note general decreasing trend in k with increasing X for these three data sets.

pressurization, and therefore were free of the corundum grains that coated the pre-pressurization grain margins of the starting mixture. While we cannot offer a simple model to explain the pore distribution in these samples, it is clear that the pore network does transmit fluid comparably to the other samples. The reader is urged to view these data cautiously because of the unconstrained effect of grain-boundary pinning on the pore network.

4.2. Textural equilibrium and thermodynamic metastability

Although thermodynamic calculations based on high T and P experimental data indicate that corundum in the presence of quartz should be consumed to make kyanite at 850 °C, 1.4 GPa (e.g. [34]), only the high X and ϕ corundum-added materials contain aluminosilicate (DcJ and Dc17). This lack of aluminosilicate at low ϕ is also seen in experiments by Harlov and Milke [35], where kyanite was found in the pores of quartz–corundum materials only if aqueous fluid exceeds 2 wt.% of the system. These authors inferred that sluggish kyanite nucleation kinetics stabilizes corundum+quartz at "dry" conditions. Similarly, aluminosilicate precipitates in our experiments exceeding ~2 wt.% fluid, but only for the samples with $X>0.018$.

While the textural development processes are remarkable, and while the presence of corundum versus aluminosilicate does significantly affect the final texture of the run product (e.g. aluminosilicate grains coarsen faster than corundum grains), the composition of the minor phase is not crucial to this investigation. Our principal goal was to fabricate largely monomineralic materials with small volumes of a minor mineral and fluid. In our materials, both corundum and aluminosilicate exhibit highly tabular morphologies, are well distributed, and are principally located adjacent to and inside of pores. Consequently, fluid flow is likely to be influenced by either of these minerals to roughly the same degree. Only the low ϕ, high X runs, Dc19 and DcM, are possible exceptions; grain boundary pinning in these two samples prohibited extensive coarsening of the irregular grains in the starting material to equant forms, perhaps producing a different pore network distribution that seen in the other samples.

4.3. The permeability–porosity relationship

Our data suggest that materials with a volumetrically minor mineral (1) exhibit different structures than those without, (2) show essentially the same fundamental relationship between permeability and porosity as do monomineralic materials (e.g. [15]), but (3) exhibit a significant reduction in permeability with increasing X. These conclusions imply that fluid transport in these materials is controlled by the same interfacial energy mechanisms at work in simpler materials. The addition of a volumetrically minor phase changes the interfacial energy conditions and as such, alters the structure (this is particularly apparent in the high X/ϕ samples).

As previously stated, the key structural control on permeability is the minimum cross-sectional area of the pore network. In the ideal case, the smallest section of the pore network is the midplane of the edge pore (see Fig. 2). That is the smallest section of the edge pore (bounded by three grains) between two corner pores (bounded by four or more grains). In monomineralic materials with a distribution of pore sizes there exists a wider distribution of minimum pore areas. These may be along the grain edges but most are probably off of the midplane.

In our materials, the pore distribution on a scale of many grains is undoubtedly similar to that of monomineralic materials. The added minor mineral reduces permeability by decreasing the minimum cross-sectional area of the edge-pores or by reducing the pore-throat area elsewhere. At least three mechanisms could contribute to edge-pore cross-sectional area reduction: (1) increasing the dihedral to or past the critical value of 60° (the edge pore will close below ϕ_c), (2) increasing faceting, which may isolate corners by reducing curvature along edges (this is a similar effect to increasing θ), and (3) reducing the volume along grain edges by concentrating the fluid at the corner pores. Reduction of the pore-throat may happen elsewhere in the pore network if the minor mineral obstructs pores, such that the cross-sectional areas of these clogged pores are smaller than those along unobstructed edges.

There are two assumptions made in invoking such simple controls on k within our data set: (1) that phlogopite, corundum, aluminosilicate, or any other volumetrically minor phase affect k to the same

degree, and that (2) the irregular texture within the low ϕ, highest X corundum runs does not independently affect k. It should be further noted that the permeability of our materials is not always lower than relative to that of pure quartzite (i.e. $X=0.0$) for a given fluid fraction (see Fig. 7). A few of our low X, low ϕ materials exhibit k higher than that predicted by Eq. (3).

4.3.1. Dihedral angle

It is unlikely that differences in θ produce the changes in k observed within our sample set. The median dihedral angles for our materials are fairly constant within $2°$ for a given material ($37°$ for phlogopite-added, $34°$ for corundum-added), so there is no obvious correlation between X and median θ. Furthermore, these values of θ are well below the critical angle and less than those determined for synthetic quartzite in Wark and Watson [16]. Such a reduction of θ would increase k, although not strongly. The calculations of von Bargen and Waff [15] predict that permeability increases by less than a factor of two as the dihedral angle decreases from $50°$ to $20°$, and Wark and Watson [16] noted no systematic permeability difference between brine–quartz materials with $\theta=38°$ and H_2O–quartz materials with $\theta=44°$.

4.3.2. Faceted pores

There is little evidence to suggest that the facets along pore boundaries, observed in all but the lowest ϕ products, substantially affect permeability. From a theoretical standpoint, the effects of faceting are unclear. Waff and Faul [36] noted pore–wall facets in synthetic dunite-melt systems and suggested that such features could enhance permeability by increasing the size of the minimum cross-sectional area of the edge pores (see Fig. 9 in [36]). Conversely, Wark et al. [37] noted that faceting may also increase the relative volume of grain-corner pores, removing fluid from the edge pores, and thereby reducing the minimum cross sectional area of the pore network.

Empirical evidence suggests that the small to moderate degree of faceting exhibited within our materials does not significantly affect permeability. Faceted synthetic quartzite and pyroxene quartzite, comparable to our corundum-added materials, exhibit the same k–ϕ relationship documented by relatively non-faceted synthetic quartzites [38]. Moreover, our materials show no relationship between permeability and faceting despite an appreciable difference in the degree of faceting between the two series (35% for Dc Series vs. 70% for Ph series). There is no correlation between the degree of faceting and X in our samples.

4.3.3. Edge pore volume reduction

Perhaps the most visible difference between our samples and those of Wark and Watson [16] is that a significant number of our pores host a minor mineral. Except for those materials with the large X/ϕ, the minor mineral is in or adjacent to the largest pores, most of which are corner pores, while the smallest pores are free of the minor mineral. At higher ϕ, the minor mineral grains form porous clusters in the larger pores. Such a distribution follows the energy constraints of a polycrystalline material approaching equilibrium [18], and should be anticipated in any material principally constructed of one crystalline phase with volumetrically minor crystalline and fluid phases. It is energetically favorable to distribute the volumetrically minor phases to the corners of the major phase. Increasing ϕ may enhance this effect by permitting more solute diffusion through an interconnected network.

The presence of the minor mineral in the larger pores suggests that the fluid phase may be partitioned to pores around the minor mineral phase. Watson [20] demonstrated that fluid partitions to pores adjacent to one mineral over another due to differences in fluid-crystal energetics in an equilibrated material composed of fluid and two mineral phases. Put simply, minerals surfaces with lower γ_{sf} attract more fluid. It is likely that our minor minerals concentrate the fluid to their boundaries. Such partitioning may be slight at low X but increase with the concentration of the minor mineral. Because the minor mineral is preferentially distributed to grain corners, this would reduce the volume of edge pores and consequently k.

4.3.4. Pore-throat occlusion

Despite the likelihood of partitioning and edge-pore reduction, there is no rigorous evidence to exclude that the minimum-pore area might be smaller elsewhere in the network. Casual observation of the samples reveals that many pores are partially occluded by the minor mineral. This suggests that these pores are obstructed; any obstruction would reduce k, and

that the degree of obstruction would correlate with X. Clusters of minor minerals obstructing larger pores are themselves porous, and many of these pores within the clusters appear smaller than the minimum cross-section of the quartz triple junctions in the same sample (admittedly difficult to constrain with two-dimensional sections). Moreover, because these pore clusters are extensively faceted (>90%), they may be appreciably impermeable regardless of pore-size, as facets intersect to isolate pores. It is therefore likely that the reduction in permeability may be the result of pore occlusion by the minor mineral, grain-edge pore volume reduction due to fluid-partitioning, or a combination of both.

5. Summary

This study produced corundum-, aluminosilicate-, and phlogopite-bearing synthetic quartzites equilibrated with an aqueous fluid, with ϕ ranging from 0.014 to 0.088. These exhibited substantially different pore geometries relative to previous evaluations of simpler systems that examined permeability–porosity relationships in pore networks. In general, the materials of this study contained a higher degree of variable faceting, a slightly lower dihedral angle, and the presence of a minor mineral phase within the pores of the major mineral phase.

The permeabilities of these materials are similar to those of pure quartzite (i.e. no minor mineral), yet more erratic with a decrease in permeability for a given fluid fraction as a function of the minor mineral volume fraction. The cause of the departure is difficult to access with the materials of this study, but is likely due to the occlusion of pores by the minor mineral, the partitioning of the fluid phase to surfaces of the minor minerals, or a combination of both processes. Additional departure at high X/ϕ may be due to pinning of grain boundaries by the minor mineral, resulting in a unique pore-structure that further limits connectivity.

The results of this study suggests that the original relationships between fluid fraction and permeability first explored numerically by von Bargen and Waff [15], and confirmed experimentally by Wark and Watson [13] and Liang et al. [14], still hold for increasingly complex materials. Only slight modification is required in addressing the presence of a volumetrically minor phase.

References

[1] E.B. Watson, J.M. Brenan, Fluids in the lithosphere: 1. Experimentally-determined wetting characteristics of CO_2–H_2O fluids and their implications for fluid transport, host-rock physical properties, and fluid inclusion formation, Earth Planet. Sci. Lett. 85 (1987) 497–515.

[2] G. Hirth, J. Tullis, The effects of pressure and porosity on the micromechanics of the brittle–ductile transition in quartzite, J. Geophys. Res. 94 (1989) 17825–17838.

[3] J. Renner, B. Evans, G. Hirth, On the rheologically critical melt fraction, Earth Planet. Sci. Lett. 181 (2000) 585–594.

[4] J.D. Bredehoeft, D.L. Norton, Mass and energy transportation in a deforming earth's crust, in: J.D. Bredehoeft, D.L. Norton (Eds.), The Role of Fluids in Crustal Processes, National Academy Press, Washington, DC, 1990, pp. 27–41.

[5] D. McKenzie, The generation and compaction of partially molten rock, J. Petrol. 25 (1984) 713–765.

[6] M. Spiegelman, D. McKenzie, Some remarks on the movement of small melt fractions in the mantle, Earth Planet. Sci. Lett. 95 (1987) 53–72.

[7] D.R. Scott, D.J. Stevenson, A self-consistent model of melting, magma migration, and buoyancy-driven circulation beneath mid-ocean ridges, J. Geophys. Res. 94 (1989) 2973–2988.

[8] G.N. Riley Jr, D.L. Kohlstedt, Kinetics of melt migration in upper mantle-type rocks, Earth Planet. Sci. Lett. 105 (1991) 500–521.

[9] B.J. Wood, J.V. Walther, Fluid flow during metamorphism and its implications for fluid–rock ratios, in: J.V. Walther, B.J. Wood (Eds.), Fluid–Rock Interactions during Metamorphism, Advances in Physical Geochemistry, vol. 5, Springer-Verlag, New York, 1986, pp. 89–108.

[10] J.E. Nielson, J.S. Noller, Processes of mantle metasomatism; Constrains from observations of composite peridotite xenoliths, in: E.M. Morris, J.D. Pasteris (Eds.), Mantle Metasomatism and Alkaline Magmatism, Geol. Soc. Am. Spec. Pap. 215 (1987) 61–76.

[11] C.S. Smith, Grains, phases, and interfaces: an interpretation of microstructure, Trans. Metall. Soc. 175 (1948) 15–51.

[12] C.S. Smith, Some elementary principles of polycrystalline microstructure, Metallurg. Rev. 9 (1964) 1–48.

[13] W.D. Kingery, H.K. Bowen, D.R. Uhlmann, Introduction to Ceramics, John Wiley & Sons, New York, NY, 1976, 1032 pp.

[14] Y. Liang, J.D. Price, D.A. Wark, E.B. Watson, Nonlinear pressure diffusion in a porous medium: approximate solutions with applications to permeability measurements using transient pulse decay method, J. Geophys. Res. 106 (2001) 529–535.

[15] N. von Bargen, H.S. Waff, Permeabilites, interfacial areas, and curvatures of partially-molten systems: results of numerical computations of equilibrium microstructures, J. Geophys. Res. 91 (1986) 9261–9276.

[16] D.A. Wark, E.B. Watson, Grain-scale permeabilities of texturally equilibrated, monomineralic rocks, Earth Planet. Sci. Lett. 164 (1998) 591–605.

[17] F.A.L. Dullien, Porous Media: Fluid Transport and Pore Structure, Academic Press, San Diego, CA, 1992, 574 pp.

[18] E.B. Watson, E.P. Vicenzi, R.P. Rapp, Inclusion/host relationships involving accessory minerals in high-grade metamorphic and anatectic rocks, Contrib. Mineral. Petrol. 101 (1989) 220–231.

[19] M.B. Holness, Surface chemical controls on pore-fluid connectivity in texturally equilibrated materials, in: B. Jamtveit, B.W.D. Yardley (Eds.), Fluid Flow and Transport in Rocks, Chapman & Hall, New York, NY, 1997, pp. 149–170.

[20] E.B. Watson, Lithologic partitioning of fluids and melts, Am. Mineral. 84 (1999) 1693–1710.

[21] D.A. Hewitt, D.R. Wones, Experimental phase relations of the micas, in: S.W. Bailey (Ed.), Micas, Miner. Soc. Am. Rev. Mineral 13 (1984) 201–256.

[22] W.F. Brace, J.B. Walsh, W.T. Frangos, Permeability of granite under high pressure, J. Geophys. Res. 73 (1968) 2225–2236.

[23] H.J.G. Gundersen, E.B. Jensen, Particle sizes and their distributions estimated from line- and point-sampled intercepts, including graphical unfolding, J. Microsc. 131 (1983) 291–310.

[24] J.C. Russ, Computer Assisted Microscopy, Plenum, New York, NY, 1990, 453 pp.

[25] I.M. Lifshitz, V.V. Slyozov, The kinetics of precipitation from supersaturated solutions, J. Phys. Chem. Solids 19 (1961) 35–50.

[26] C. Wagner, Theorie der Alterung von Niedrschlaegen durch Umloesen (Ostwald Reifung), Zeitsch, Elektrochemie 65 (1961) 581–591.

[27] J.L. Joesten, Kinetics of coarsening and diffusion-controlled mineral growth, in: D.M. Kerrick (Ed.), Contact Metamorphism, Miner. Soc. Am. Rev. Mineral., vol. 26, 1991, pp. 507–582.

[28] A.K. Galwey, K.A. Jones, An attempt to determine the mechanism of a natural mineral-forming reaction from examination of the products, J. Chem. Soc., London (1963) 5681–5686.

[29] A. Belonoshko, S.K. Saxena, A molecular dynamics study of the pressure–volume–temperature properties of super-critical fluids: I. H_2O, Geochim. Cosmochim. Acta 55 (1991) 381–387.

[30] C.J.L. Wilson, The prograde microfabric in a deformed quartzite sequence, Mount Isa, Australia, Tectonophysics 19 (1973) 39–81.

[31] J.F.M. Hippert, Grain boundary microstructures in micaceous quartzite: significance for fluid movement and deformation processes in low metamorphic grade shear zones, J. Geol. 102 (1994) 331–348.

[32] D.L. Olgaard, B. Evans, Grain growth in synthetic marbles with added mica and water, Contrib. Mineral. Petrol. 100 (1988) 246–260.

[33] J. Tullis, R.A. Yund, Grain growth kinetics of quartz and calcite aggregates, J. Geol. 90 (1982) 301–318.

[34] D.E. Harlov, R.C. Newton, Reversal of the metastable kyanite+corundum+quartz and andalusite+corundum+quartz equilibria and the enthalpy of formation of kyanite and andalusite, Am. Mineral. 78 (1993) 594–600.

[35] D.E. Harlov, R. Milke, Stability of corundum+quartz relative to kyanite and sillimanite at high temperature and pressure, Am. Mineral. 87 (2002) 424–432.

[36] H.S. Waff, U. Faul, Effects of crystalline anisotropy on fluid distribution in ultramafic partial melts, J. Geophys. Res. 97 (1992) 9003–9014.

[37] D.A. Wark, E.B. Watson, C.C. Williams, J.D. Price, Reassessment of pore shapes in microstructurally equilibrated rocks, with implications for permeability of the upper mantle. J. Geophys. Res. (in press).

[38] J.D. Price, D.A. Wark, E.B. Watson, Permeability of the lower crust and upper mantle: conclusions from complex synthetic rocks, EOS, Trans. Am. Geophys. Soc. 82 (20) (2001) Abstract V41 C-03.